

# Dendritic Spacing/Columnar Grain Diameter of Al–2Mg–Zn Alloys Affecting Hardness, Tensile Properties, and Dry Sliding Wear in the As-Cast/Heat-Treated Conditions

Carolina Ache, Maiquel Lopes, Bernardo Reis, Amauri Garcia, and Carlos dos Santos\*

Inter-relations of solidification conditions, as-cast and heat-treated structures, and mechanical properties are extremely useful in the design of components, especially Al-based alloys. Herein, the effects of secondary dendrite arm spacing ( $\lambda_2$ ) and columnar grain diameter (CGD) on hardness, tensile, and dry sliding wear responses of Al–2Mg–(5 and 8)Zn (wt%) alloys in the as-cast and heat-treated conditions, respectively, are focused upon. The alloys are melted and solidified in an instrumented upward directional solidification apparatus under nonsteady-state heat transfer conditions. Samples are cut from the solidified ingots and subjected to the T6 heat treatment. Samples are characterized metallographically by optical and scanning electron microscopies and mechanically by Brinell hardness, tensile, and dry sliding wear tests. It is found that higher Zn concentration and solidification cooling rates refine  $\lambda_2$  and the CGD. Hardness and tensile properties are improved with the decrease in  $\lambda_2$  in the as-cast condition of both alloys. After heat treatment, all these properties increase with the decrease in CGD. Wear parameters show that only the alloy having a higher Zn content is associated with better wear resistance. Correlations between the wear rate as a function of  $\lambda_2$  and CGD are established by experimental equations.

artificial aging steps. The solutionizing process aims at the dissolution of precipitates and intermetallic (IMC) particles in an  $\alpha$ -Al solid solution, to obtain a supersaturated solid solution (SSSS<sub>0</sub>), after quenching. During the aging process, Engdahl et al. have discussed a sequence of transformations that can occur in Al–Zn–Mg alloys depending on the Zn:Mg ratio.<sup>[1]</sup> In general, two types of Guinier–Preston (GP) zones are initially noted, the GP II and the GP I zones, which are zones containing a few atoms of solute on {111}-Al planes and {100}-Al planes, respectively, followed by a metastable precipitate ( $\eta'$ ) and finally, by the equilibrium phase ( $\eta$ ). Belov et al. detailed that the latest phase is expected to have a composition MgZn<sub>2</sub> at equilibrium, known as the C14-Laves phase, with a hexagonal structure.<sup>[2]</sup>

The microstructure evolution during precipitation hardening and the resultant mechanical properties are extensively described in the literature for the wrought Al-based hardenable alloys. Dumont et al.


studied the effect of different quench rates and heat treatment parameters on the microstructural evolution, strength, and toughness responses of an Aluminum Association 7050 Al alloy.<sup>[3]</sup> The experimental results confirmed that the quench rates after solutionizing have a major impact on the size and distribution of the precipitates, a moderate effect on yield strength, and a dominant effect on notch resistance. Gubicza et al. examined the influence of high plastic strain at high temperature on microstructural evolution in different Al–Zn–Mg alloys subjected to solution heat treatment.<sup>[4]</sup> According to the authors, plastic deformation after solutionizing promoted grain refining and  $\eta$  phase precipitation, indicating that the stages of the GP zone formation is suppressed.<sup>[4]</sup> The influence of the precipitated particles on the mechanical properties is explained by the Orowan mechanism, where these particles reduce the dislocation mobility inside the grains during plastic deformation, consequently leading to increase in strength and decrease in ductility, as discussed by Zander and Sandstrom, based on the results obtained from mathematical models coupling thermodynamic data and strength models.<sup>[5]</sup> In the case of as-cast Al–Zn–Mg alloys, aspects such as casting processes and microstructure features have been analyzed by Acer et al. to understand the material interactions and their final mechanical properties after heat

## 1. Introduction

Al–Zn–Mg alloys have an excellent combination of properties such as high mechanical strength, toughness, corrosion resistance, and low density and melting point, making them one of the most important aluminum alloys for engineering applications. These alloys are utilized in the wrought or as-cast conditions, and when improved mechanical properties are required, precipitation-hardening heat treatments can be performed. These heat treatments include solutionizing and natural or

C. Ache, M. Lopes, Dr. B. Reis, Prof. C. Santos  
School of Technology  
Pontifícia Universidade Católica do Rio Grande do Sul – PUCRS  
Av. Ipiranga, 6681, Porto Alegre, RS 90.619-900, Brazil  
E-mail: carlos.santos@pucrs.br

Prof. A. Garcia  
School of Mechanical Engineering  
University of Campinas – UNICAMP  
Av. Zeferino Vaz, Campinas, SP 13083-860, Brazil

 The ORCID identification number(s) for the author(s) of this article can be found under <https://doi.org/10.1002/adem.201901145>.

DOI: 10.1002/adem.201901145

treatments.<sup>[6]</sup> The authors determined the optimum heat treatment parameters for solution and aging processes (in terms of temperature and time) to improve hardness and tensile properties as a function of the as-cast microstructures of the Al–5.5Zn–2.5Mg alloy (wt%).<sup>[6]</sup> The highest strength responses were attained at higher homogenization and aging temperatures, 475 and 150 °C, respectively, both during the 24 h period. The best behavior was attributed to the finer distribution of the precipitates after heat treatment. The study presented by Isadare et al. showed a comparison between annealing and age-hardening heat treatments of the as-cast 7075 Al alloy (Al–5.6Zn–2.5Mg–1.6Cu–wt%) solidified under different cooling rates.<sup>[7]</sup> Slower cooling generated coarser precipitates, whereas fast cooling showed finer and dispersed precipitates. In general, the strength responses were enhanced and ductility decreased after the precipitation-hardening heat treatment, mainly for refined microstructures.

Regarding the wear behavior, Prasada Rao et al. showed that wear resistance improves with the decrease in the grain size, following a linear trend of as-cast pure Al.<sup>[8]</sup> This demonstrates that in the absence of second phases, mechanical strength improvement is directly associated with the increase in the grain boundary densities. In the case of binary alloys, Lepper et al. developed an extensive investigation of Al–Sn-, Al–Bi-, and Al–Pb-bearing alloys solidified under magnetic and electric fields.<sup>[9]</sup> Using a pin-on-disc apparatus, dry sliding wear tests were performed in air and in vacuum environments. They found that the environment has a more pronounced influence on the wear responses than chemical compositions and microstructures for the analyzed alloys. Recent studies have reported the role of the inter-relations of solidification conditions, cellular spacings, primary/secondary dendrite arm spacings, and wear behavior in binary and ternary aluminum-based alloys.<sup>[10–21]</sup> According to these investigations, the wear behavior is considerably affected by the scale, morphology, and distribution of the cellular and/or dendritic networks inside the grain structure, as well as their tribological characteristics. Although many researches correlating metallurgical aspects with wear behavior can be found in the literature, information on the effects of heat treatments of as-cast Al–Zn–Mg alloys on wear resistance is still scarce in the literature, mainly when searching to establish correlations between solidification parameters, microstructure evolution, heat treatments, and wear behavior. A remarkable study was conducted by Rao et al. to examine the effect of age hardening on the wear resistance of as-cast Al–Zn–Mg alloy, however, reinforced with silicon carbide (SiC) hard particles.<sup>[22]</sup> In addition to the  $\alpha$ -Al matrix and the IMC precipitates in the interdendritic regions, SiC particles were distributed in the matrix. After heat treatment, sliding wear response improved due to matrix hardening, as well as the presence of hard particles. The distribution, size, and morphology of the IMC compound, as a consequence of the alloy Zn–Mg ratio, are fundamental in achieving the solutionizing and aging steps during heat treatment, as the addition of Zn to Al–Mg alloys has a significant influence on the as-cast microstructure, mainly when considering the formation of the MgZn<sub>2</sub> second phase. An increase in MgZn<sub>2</sub> formation during solidification due to a higher alloy Zn content and controlled precipitation during the aging step enhance the strength properties, special hardness, and wear responses. The main objective of this work is to investigate the influence of the precipitation-hardening

heat treatment (solutionizing and artificial aging—T6) on the resulting hardness, tensile strength, and dry sliding wear response of directionally solidified Al–2Mg-(5 and 8)Zn alloys (wt%). Moreover, experimental correlations between microstructure and macrostructure parameters, hardness, tensile, and wear properties in the as-cast and post-heat-treated conditions are envisaged. Hardness and tensile strength are correlated with dendrite arm spacing in the as-cast condition and with columnar grain diameter (CGD) in the heat-treated condition. Archard's law for sliding wear rate was proposed in terms of  $\lambda_2$  and CGD in the as-cast and heat-treated conditions, respectively.

## 2. Experimental Section

The experiments were conducted with two Al–Mg–Zn alloy compositions: Al–2Mg–5Zn and Al–2Mg–Zn (wt%), labeled as 752 and 782 alloys. Pure aluminum (>99.5%) and additions of pure magnesium (>99.9%) and pure zinc (>99.7%) were used to obtain the required alloy concentrations. Melting was conducted in an electric resistance soak furnace using a silicon carbide crucible and a stainless-steel bar stirrer, both protected with boron nitride coating. After melting, samples were extracted for chemical composition analyses by optical emission spectroscopy (OES). **Figure 1a** shows the partial Al–2Mg–Zn (wt%) phase diagram simulated by the Thermo-Calc software, as well as the average values of the measured chemical composition of each examined alloy, as indicated by the vertical dotted lines in the phase diagram.

The alloys were remelted in situ in a solidification apparatus that allows vertical upward directional solidification under transient heat flow conditions (**Figure 1b**). The main design criterion was to ensure a dominant unidirectional heat flow condition during solidification. In addition, the experimental setup permitted natural convection to be minimized, improved solute distribution in the liquid, and induced a close contact between the metal and internal mold surface during solidification. A cylindrical SAE 1020 steel mold (110 mm diameter; 140 mm height) was used and water cooled at the bottom. K-type thermocouples were positioned at 6, 12, 18, 24, 30, and 50 mm from the internal cooled surface of the mold to record the thermal responses during solidification. The alloys were melted at 720 °C  $\pm$  7 °C and solidified using a water flow of 4 L min<sup>−1</sup> on the bottom of the mold, permitting tip growth rates during solidification ranging from 0.37 to 0.21 mm s<sup>−1</sup> and liquid thermal gradients from 13<sup>1</sup> to 2 °C mm<sup>−1</sup> for those positions from the bottom to the top of the ingots. The details of the casting assembly and procedures have been described in our previous work.<sup>[23]</sup> However, in this investigation, the ingots were solidified under higher cooling rates due to a more efficient cooling system; consequently, the obtained microstructures were more refined than those previously observed. As the as-cast microstructure has a strong influence upon heat treatment responses, it was necessary to characterize the microstructure features as a function of the specific solidification conditions, correlating to the subsequent heat treatments and resultant properties.

In this study, three identical solidified ingots were obtained for each alloy, one for as-cast analyses and two for heat treatment investigations. Initially, transversal discs with 20 mm thickness were extracted from one alloy ingot at the positions 12, 30, and

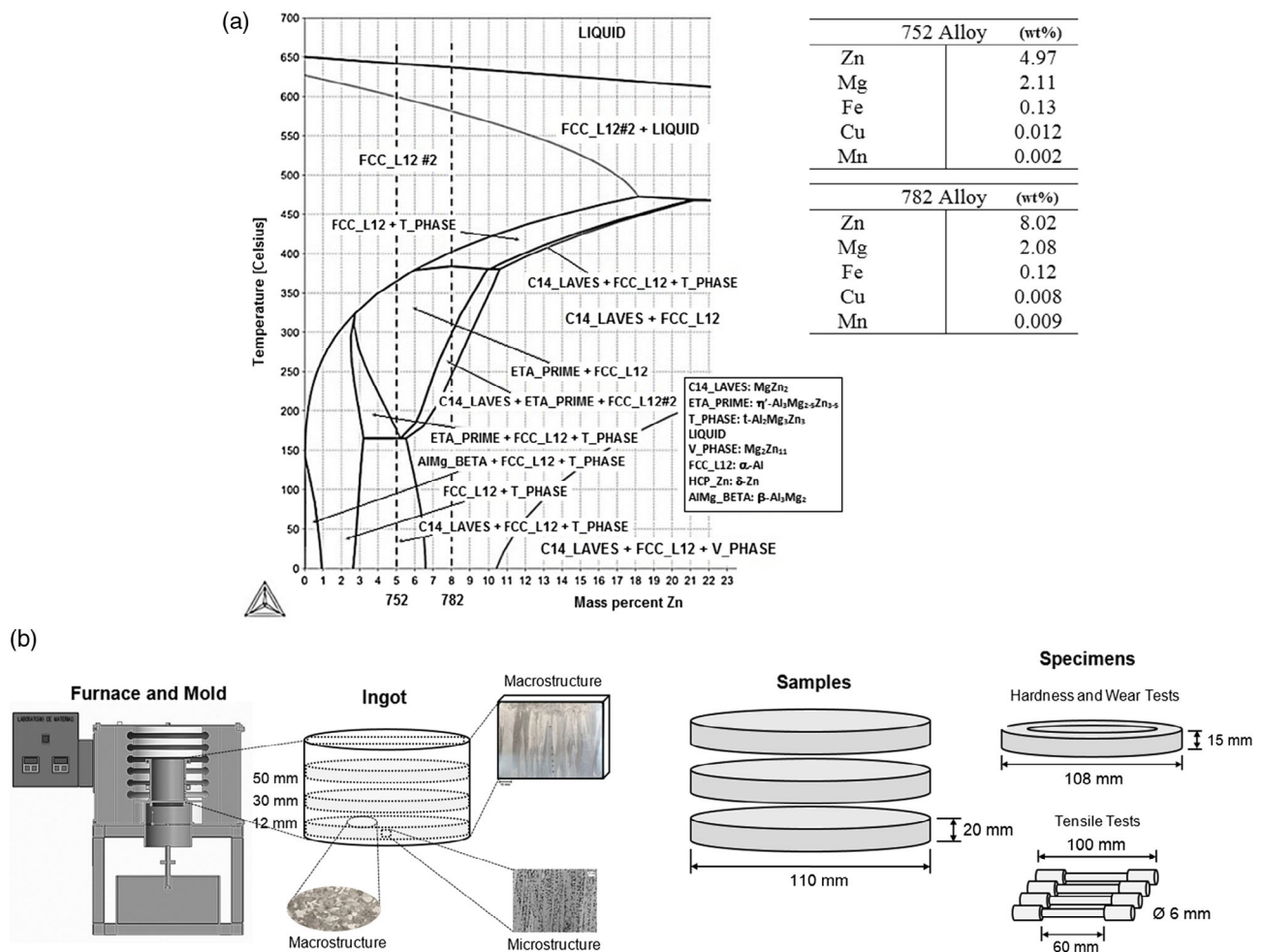


**Figure 1.** a) Partial Al–Mg–Zn phase diagram and chemical compositions of the examined alloys and b) directional solidification setup, samples, and specimens.

50 mm for further heat treatment (solutionizing and artificial aging—T6). Heat treatments were performed to analyze the dissolution of the MgZn<sub>2</sub> IMCs in the α-Al matrix as a function of temperature and time. Samples (15 × 15 mm) extracted from the discs were heated in the range 450–540 °C for 30–360 min for solutionizing, followed by artificial aging in the range 130–190 °C for 60–300 min. The ideal conditions in terms of temperature and time for solutionizing (470 °C–180 min) and artificial aging (150 °C–240 min) were selected as the precipitation-hardening parameters to be applied in the reserved ingot of each alloy.

The microstructural characteristics in the as-cast and post-heat-treated conditions were compared in longitudinal and transverse sections of the samples. The modified Keller's reagent was used for revealing the macrostructure (etching time: 60 s) and microstructure (etching time: 10 s), according to ASTM E3, ASTM E407, and ASTM E112.<sup>[24–26]</sup> The microstructures of as-cast and heat-treated samples were examined by optical microscopy. Brinell hardness (HB) was measured in the transverse sections of the samples according to the ASTM E10 standard test method.<sup>[27]</sup>

A pin-on-disc device was used for dry sliding wear tests on the surface of the discs, as prescribed by ASTM Standard G99.<sup>[28]</sup>

Two analyses were performed with each disc (on both faces of the discs extracted from the samples, with a diameter of 108 mm and thickness of 15 mm). Before the wear tests, the discs were ground on both faces with sandpapers (superficial roughness <0.8 mm), cleaned, and air dried. Alumina ceramic balls (10 mm diameter) were used as the counterface material due to their higher hardness (1500 HV) in comparison with those of the alloys, restricting surface damage of the pin. For all wear tests, identical parameters to those used in our previous work were adopted (14.7 N normal load, 1.8 m s<sup>-1</sup> sliding speed, and 1000 m total sliding distance) for comparison purposes.<sup>[23]</sup> The parameters were selected for inducing high stress (Hertzian contact pressure—750 MPa maximum—higher than the alloy yield strengths), severe wear damage in the disc, and high-speed contacts for preventing excessive wear-track heating; similar conditions to those found in structural components of automobile suspension parts. Each wear test was conducted in duplicate, resulting in four analyses per disc. After the first set of tests, discs were machined to remove a 3 mm-thick layer of material in each face. After machining, surface preparation followed the same procedure described earlier. For the wear-track width, eight

measurements were carried out for each 100 m sliding distance in locations 45° from each other along the sliding path. The average values of these measurements were used to determine the disc wear-volume loss according to the equation proposed by ASTM G99.<sup>[28]</sup>

The tensile test specimens were prepared according to ASTM Standard E8/E8M–16a.<sup>[29]</sup> Four specimens were taken from transverse discs of each alloy ingot at different locations from the cooled bottom of the casting (12, 30, and 50 mm), and average values were determined. Figure 1b shows the solidification apparatus and the methodologies for extraction of the samples/specimens for metallography analyses and mechanical testings.

### 3. Results and Discussion

#### 3.1. As-Cast Conditions: Microstructure; Secondary Dendritic Arm Spacing; Macrostructure; and CGD

The cooling curves acquired during the solidification of alloys and corresponding to the thermocouple locations (6, 12, 18,

24, 30, and 50 mm) were used to determine the position of the Liquidus isotherm ( $T_L$ ) as a function of time ( $t_L$ ), as shown in **Figure 2a**. As a set of solidification experiments was conducted for each alloy, it is fundamental to determine the solidification parameters to ensure the repeatability of results. Error bars associated with Liquidus isotherm time for the three solidified ingots of each alloy are shown in the graph, demonstrating that the variation is acceptable (<5%). The cooling rates ( $\dot{T} = \frac{dT}{dt}$ ) were calculated by deriving the temperature with respect to time, immediately after the passing of the Liquidus isotherm by each position, and the results are shown in **Figure 2b**. The solidification macrostructures of the resulting ingots showed a predominant columnar zone along the ingots, consisting of elongated grains with direction close to the heat flow direction, as shown in **Figure 2c,d**.

The morphology of the Al-rich phase was shown to be characterized by a dendritic network.  $\lambda_2$  increases with the decreasing cooling rate at positions far away from the cooled bottom of the mold for both alloys. The smallest values were observed for the 782 alloy, at regions near the bottom of the ingot, whereas

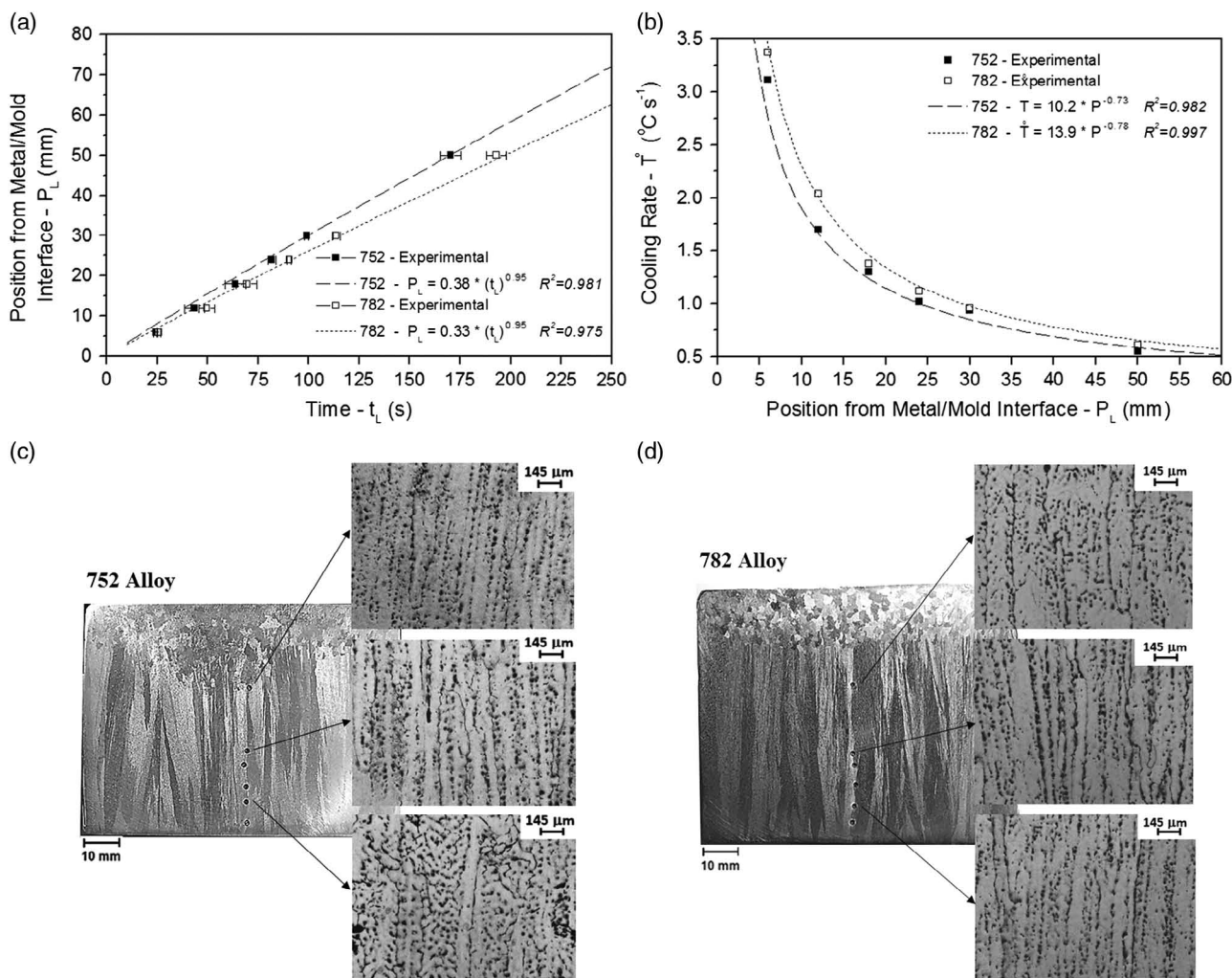


**Figure 2.** a) Position of the Liquidus isotherm as a function of time, b) cooling rate variation with position along the solidified ingots;  $R^2$  is the coefficient of determination, c) longitudinal macrostructures, and d) longitudinal microstructures of the 752 and 782 alloys ingots.

the highest values were noted for the 752 alloy close to the top of the ingot. The behavior of samples of the 782 alloy having smallest  $\lambda_2$  (as compared with similar samples of the 752 alloy) can be attributed to the higher alloy solute content, which promotes refining in the secondary dendrite arms due to solute segregation during solidification, as well as higher solidification cooling rates.

As reported by Reis et al., results of scanning electron microscopy–energy-dispersive X-ray spectroscopy (SEM–EDS) analyses and X-ray diffraction (XRD) confirmed that both alloys have microstructures consisting of the dendritic matrix of  $\alpha$ -Al with C14-Laves  $MgZn_2$  and  $\tau$ -phase  $Al_2Mg_3Zn_3$  precipitates in interdendritic spacings.<sup>[23]</sup> Despite the phase equilibrium diagram of Figure 1a, which predicts only the presence of  $\alpha$ -Al and C14-LAVES phases at low temperatures, the  $\tau$  phase precipitates as a consequence of solidification occurs under nonequilibrium cooling conditions in the present experiments that restrict the diffusion of the alloying elements into the  $\alpha$ -Al matrix, which remained segregated in the liquid phase. These results are in agreement with those reported by Raghavan<sup>[30]</sup> based on the computed phase diagrams for Al–Zn–Mg alloys, with the microstructural characterization performed by Alvarez et al. and Soto et al. of as-cast alloys containing higher Zn and Mg contents and with the solute distribution obtained by microanalyses in an Al–5.3Zn–5.3Mg alloy (wt%), as described by Ramirez-Ledesma et al.<sup>[31–33]</sup>

The Zn and Mg profiles in the castings were investigated and determined by optical emission spectrometry analyses conducted in each transversal disc sample, as shown in Figure 1b. For each position, 12 measurements were carried out, and the average values are shown in Figure 3a. As shown, no evidence of macrosegregation was detected in the Zn and Mg profiles, and the nominal composition deviation was noted to be less than 0.2 wt% for both alloying elements, as indicated by the error bars.

The secondary dendrite arm spacing ( $\lambda_2$ ) was measured (20 measurements for each position) along the length of the ingot with a view to examine the evolution of the dendritic length scale. The results as a function of the cooling rate along the ingot are shown in Figure 3b. The intercept method was applied to determine the average CGD in the ingots transverse sections located at 12, 30, and 50 mm from the cooled bottom and

correlated with the solidification cooling rate during solidification. For each position, at least 20 CGD measurements were carried out, and the average, minimum, and maximum values are shown in Figure 3b. At high cooling rates, near the cooled bottom of the ingots, the CGDs are very similar for both alloys, indicating that the influence of high cooling rates prevailed over that of the solute content in the grains nucleation. As the distance from the metal/mold interface (cooled bottom of the ingots) increases and the cooling rate decreases, the 782 alloy showed CGDs that are smaller than those of the 752 alloy, due to the higher alloy Zn content that prevails over the influence of the cooling rate. When analyzing the evolution of  $\lambda_2$ , the results are shown to be quite similar to those obtained in the previous investigation described by Reis et al., indicating that a single power function with a  $-1/3$  exponent can be used to express the variation of  $\lambda_2$  versus cooling rate for both alloys, as initially suggested by Bouchard and Kirkaldy and confirmed by Quaresma et al. for the binary Al–4Cu and Al–15Cu (wt%) alloys solidified in a horizontal directional apparatus, Spinelli et al. for downward unsteady-state directionally solidified Al–Cu alloys, and Reis et al. for upward unsteady-state directionally solidified Al–4Cu alloy (wt%).<sup>[10–12,23,34]</sup> Similar results were obtained by Goulart et al. for binary Al–Si alloys, as well as for ternary Al–Si–Cu alloys, as reported by Costa et al., despite results of some specific ternary aluminum-based alloys, for which a better agreement was shown to occur with a  $-1/2$  exponent for Al–Cu–Ni, as found by Rodrigues et al., and for Al–Cu–Si alloys, investigated by Osório et al.<sup>[13–16]</sup>

### 3.2. Mechanical Properties of As-Cast and Post-Heat-Treated Samples

To determine the best heat treatment operational conditions in terms of temperature and time for solutionizing and artificial aging procedures, a set of experiments was performed on both alloys using samples extracted from the castings. The conditions were established based on hardness results obtained in samples at 12, 30, and 50 mm from the cooled bottom of the mold (Figure 4), and the selected conditions were determined using a statistical approach. Emphases were given to samples from

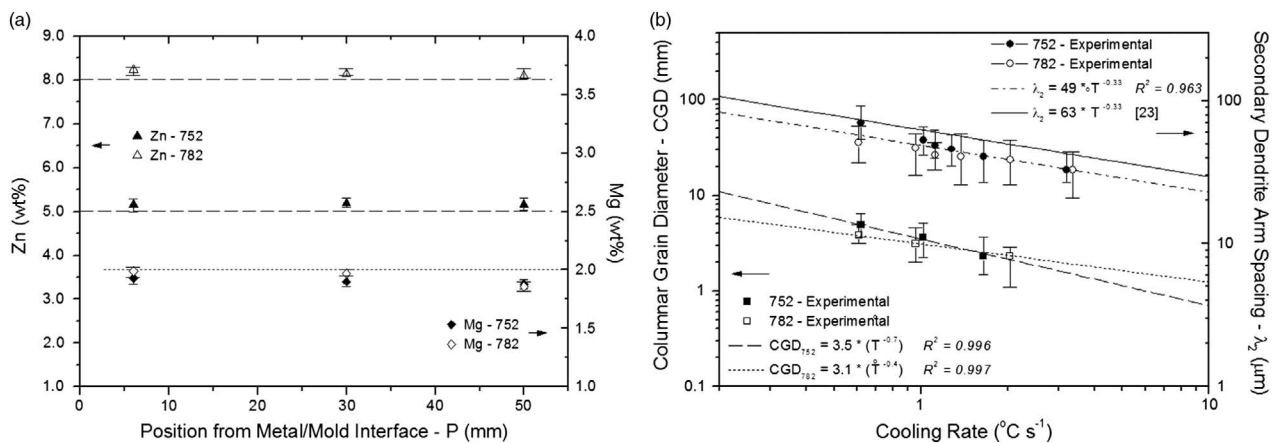


**Figure 3.** a) Zn and Mg profiles (dashed lines indicate the nominal Zn and Mg contents, ▲ and △ represent measured Zn contents, and ◆ and ◇ represent measured Mg contents) and b) CGD and  $\lambda_2$  versus cooling rate.

positions farthest from the bottom, which are associated with coarser microstructures due to lower solidification cooling rates and the 782 alloy that has a higher Zn content. The best temperature–time parameters determined for solutionizing and artificial aging heat treatments were 470 °C–180 min and 150 °C–240 min, respectively, for both alloys. These operational conditions were applied to the samples along the precipitation-hardening heat treatment.

After heat treatments, the microstructures of both alloys were composed basically of a supersaturated  $\alpha$ -Al matrix with sporadic undissolved globular particles in some locations, in particular at those interdendritic regions with larger spacings. The columnar grain size was identical to that of the as-cast samples, indicating that the solutionizing heat treatment procedure unmodified the grain size of the as-cast alloys.

The average results of HB, ultimate tensile strength (UTS), and strain to fracture ( $\delta$ ) of the as-cast and post-heat-treated specimens are shown in Table 1. As shown, the samples from the 782 alloy ingot presented a higher HB than those of the 752 alloy ingot due to the higher alloy Zn concentration and the more refined microstructure. After being subjected to heat treatments, the HB values significantly increased as compared with those of the as-cast condition, mainly for the 782 alloy, for which the hardness of the more refined sample ( $P = 12$  mm) increased to about 31%, 33% for  $P = 30$  mm, and 47% for  $P = 50$  mm. This can be attributed to the precipitation-hardening effect, which is improved with the increase in the Zn:Mg ratio, which increases the  $MgZn_2$  fraction, thus favoring the process of blocking dislocation movement

during plastic deformation by lattice distortions in the crystal structure inside the grains, as reported by Zander and Sandstrom and confirmed by Isadare et al.<sup>[5,7]</sup> The samples from positions near the cooled bottom of the mold presented higher values than those closer to the top in both as-cast and heat-treated alloys. After heat treatments, the samples were not analyzed by microscopy due to the dissolution of the dendritic morphology. The resulting UTS showed similar behavior, which increased significantly as compared with the values associated with samples in the as-cast condition (at about 32% higher for samples from positions near the bottom and 50% higher for samples near the top of the 782 alloy ingots). In the case of the strain to fracture, an opposite behavior can be observed. The as-cast 752 alloy presented the highest value near the bottom of the ingot, 132% higher than that of the as-cast 782 alloy, and this difference decreases for samples from positions closer to the top of the ingots. Changes in mechanical strength and ductility as a result of the position along the ingot are reported by Costa et al. to be associated with microstructural features.<sup>[14]</sup> The increased hardness and tensile strength are attributed to smaller  $\lambda_2$ , a more homogeneous distribution of precipitates, and smaller CGD of samples in the as-cast condition for positions closer to the bottom of the ingots. With coarsening in the structure, both the strength and ductility sharply decrease. The samples that were heat treated exhibited a moderate decrease in tensile strength and strain to fracture for all positions from the bottom to the top of the castings.

HB and tensile properties have been correlated with macrostructure and microstructure features, as shown in Figure 5.

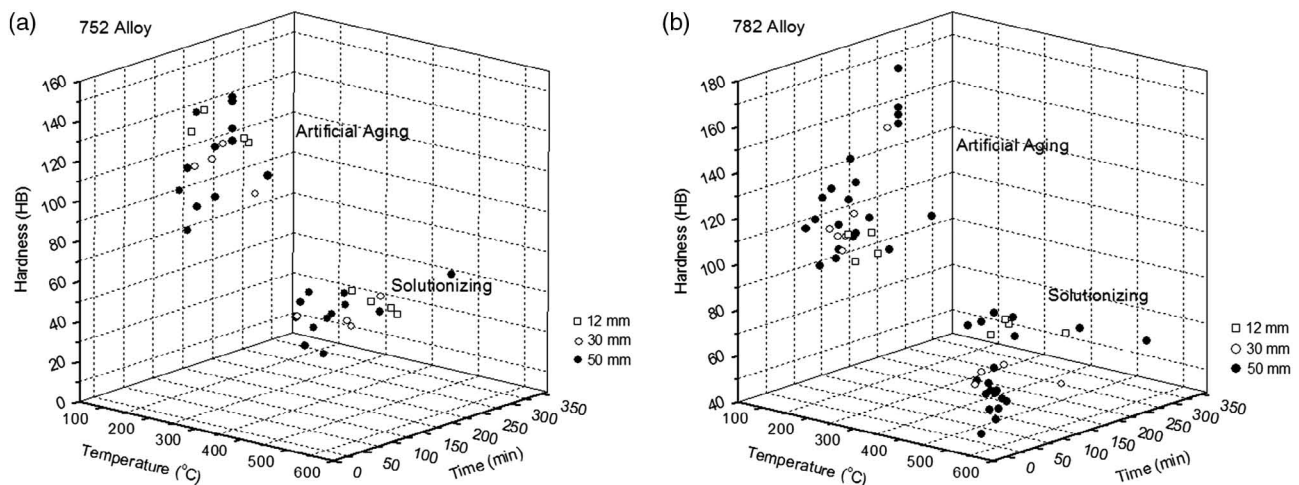


**Figure 4.** Hardness variation with temperature and time during solutionizing and artificial aging of samples from the a) 752 and b) 782 alloys ingots.

**Table 1.** Hardness, UTS, and strain to fracture of samples from the 752 and 782 alloys ingots in the as-cast and heat-treated conditions.

|               | 752 Alloy |     |     |              |     |     | 782 Alloy |     |     |              |     |     |
|---------------|-----------|-----|-----|--------------|-----|-----|-----------|-----|-----|--------------|-----|-----|
|               | As Cast   |     |     | Heat Treated |     |     | As Cast   |     |     | Heat Treated |     |     |
| Position [mm] | 12        | 30  | 50  | 12           | 30  | 50  | 12        | 30  | 50  | 12           | 30  | 50  |
| Hardness [HB] | 102       | 98  | 90  | 128          | 123 | 120 | 127       | 121 | 113 | 166          | 162 | 156 |
| UTS [MPa]     | 301       | 245 | 143 | 365          | 347 | 337 | 363       | 333 | 272 | 479          | 452 | 409 |
| $\delta$ [%]  | 11.4      | 7.5 | 3.8 | 4.5          | 2.4 | 1.3 | 4.9       | 3.6 | 2.1 | 2.0          | 1.5 | 1.1 |

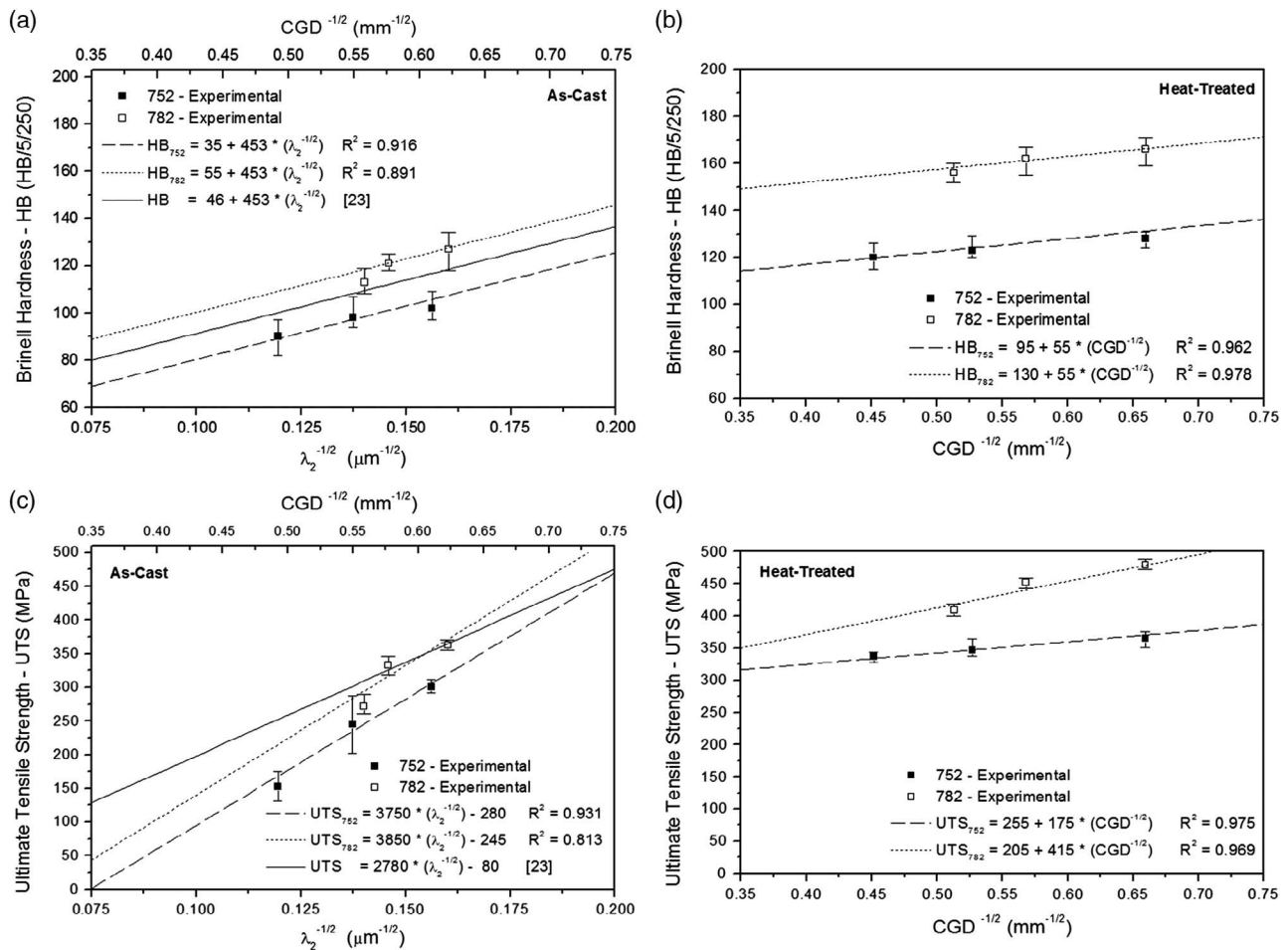


**Figure 5.** a,b) HB and c,d) UTS versus microstructure features of samples from the 752 and 782 alloys ingots in the as-cast and heat-treated conditions.

In the as-cast condition, the properties were plotted as a function of both  $\lambda_2$  and CGD. In the heat-treated condition, the properties were plotted as a function of CGD only, as during heat treatment, the dissolution of the second phase takes place, with consequent dissolution of the dendritic morphology. Experimental Hall-Petch-type expressions were obtained by a curve-fitting technique (dashed lines); in the as-cast condition, these properties are dependent on the inverse square root of  $\lambda_2$  and CGD, whereas in the heat-treated condition, this dependence is on the inverse square root of CGD. For comparison purposes, the experimental equations for HB and UTS obtained in the previous work reported by Reis et al., using the same alloys and similar experimental procedures for the as-cast condition, are shown in Figure 5a,c (solid lines).<sup>[23]</sup>

As shown in Figure 5a–d, HB and UTS increased with a decrease in  $\lambda_2$  and CGD, in both the as-cast and heat-treated conditions, respectively. With an enlargement in the alloy Zn content, HB and UTS increased. The differences in tensile strength between the 752 and 782 alloys ingots were more pronounced after heat treatments, which seems to be associated with more refined structures and in the case of the 782 alloy also with higher Zn content. With smaller dendritic spacings, the dissolution of interdendritic phases during solubilization is enhanced,

improving the matrix strength. Furthermore, the smaller grain size restricts the dislocation motion during plastic deformation. In the present investigation, specific equations for each alloy were required to express the trend of the HB and UTS experimental results, whereas in the work reported by Reis et al., a single equation represented the evolution of hardness and strength responses with  $\lambda_2$  for the alloys in the as-cast condition.<sup>[23]</sup>

Similar behaviors were observed by Acer et al. and Chemingui et al. for Al–5.5Zn–2.5Mg and Al–4.6Zn–1.2Mg (wt%) alloys, respectively, submitted to different heat treatments.<sup>[6,35]</sup>

Regarding the wear analyzes, **Figure 6** shows the disc wear-volume loss, determined according to ASTM Standard G99, using the measured wear-track width. As the alumina-pin hardness is much higher than the disc hardness, the pin-wear was insignificant.<sup>[28]</sup> Based on the approach proposed in recent works for binary Al–Sn and Al–Si alloys investigated by Cruz et al., Al–In alloys studied by Freitas et al., and for Al–Bi and Al–Pb examined by Freitas et al., as well as the works presented by Costa et al. with ternary Al–Bi–Sn alloys, Bertelli et al. with Al–Sn–(Cu–Si), and Rodrigues et al. with Al–Cu–Ni alloys, correlations between disc wear-volume loss (*V*),  $\lambda_2$ , and CGD for the as-cast and heat-treated conditions, respectively, are shown in Figure 6 for 100, 500, and 1000 m sliding distances.<sup>[15,17–21]</sup>

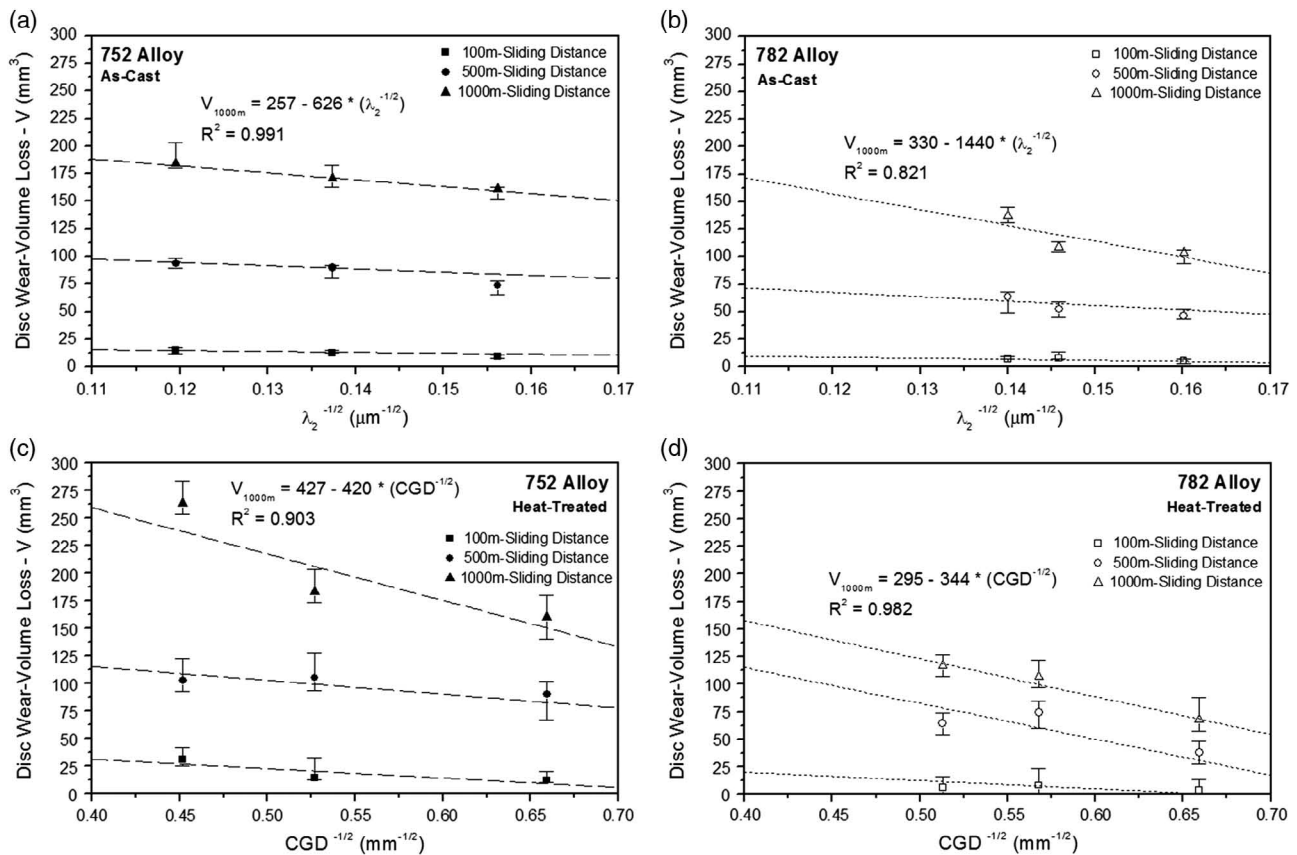


**Figure 6.** Disc wear-volume loss variation with  $\lambda_2$ , CGD, and sliding distance for: a,b) as-cast and c,d) heat-treated conditions.

The points represent the experimental results and the dashed lines refer to curve fitting to the experimental points. Hall-Petch-type expressions are also obtained for the wear-volume loss as a function of  $\lambda_2$  and CGD for 1000 m sliding distance. The wear-volume loss points to superior wear resistance for positions near the bottom of the ingot (associated with more refined structures) and worse wear resistance for positions farther from the cooled bottom (associated with coarser structures). For all examined positions, the 782 alloy presented lower wear-volume loss as compared with the corresponding positions in the 752 alloy ingot and consequently, higher wear resistance in both as-cast and heat-treated conditions. In the as-cast condition, the lower wear resistance for the 752 alloy as compared with that of the 782 alloy can be attributed to the lower hardness because of the lower alloy Zn content, the smaller amount of  $MgZn_2$  hard precipitates in the interdendritic regions, and coarser  $\lambda_2$ . With the increase in the alloy Zn content, the amount of  $MgZn_2$  increases and the size of  $\lambda_2$  decreases, improving wear response by protecting the Al matrix and avoiding the plowing of the surface. Similar behavior was observed by Prashanth et al. for Al-Si alloys tested under low loads (<20 N), where the presence of hard particles distributed along the Al matrix reduced the wear. However, this behavior can change when load or size of the particles are increased, and the hard particles can act as a plow in the surface, removing material by abrasion.<sup>[36,37]</sup> Mondal et al. noted that the addition of hard particles (SiC) in Al-Zn-Mg alloys decreases the wear rate at

lower loads due to the increase in surface roughness and decrease in the effective contact area between the surfaces.<sup>[38]</sup> An opposite wear response can be observed if the particles or second phases are softer, as demonstrated by Cruz et al. for Al-Sn alloys, Bertelli et al. for Al-Sn(Cu-Si) alloys, and Freitas et al. for Al-In and Al-Pb alloys.<sup>[17-19,21]</sup> In these studies, the higher wear resistance was associated with the higher amount and larger size of soft phases in the Al-matrix, i.e., coarser structures have shown better wear response. In contrast, results obtained by Costa et al. with Al-Bi and Al-Bi-Sn alloys indicated that not only the lower hardness of the second phases leads to increasing wear resistance (caused by the self-lubricating effect), but a more extensive distribution of Bi and Bi/Sn particles positively affects wear behavior.<sup>[20]</sup>

The wear behavior of the heat-treated samples can be associated with CGD, with lower wear-volume loss being related to samples having more refined structures and a higher Zn content (782 alloy), as shown in Figure 6. An opposite behavior was observed in the 752 alloy, where the samples in the as-cast condition showed lower wear-volume loss as compared with the observed values in the heat-treated samples, despite the higher hardness exhibited after heat treatment. This indicates that not only hardness influences the wear resistance, but also the microstructure characteristics have an important effect. Linear relationships relating  $V$  to  $\lambda_2$  and  $V$  to CGD have been derived for all analyzed conditions.



Archard's law, proposed initially by Archard and confirmed by Archard and Hirst, which correlates the wear rate ( $W$ ) with the wear coefficient ( $k$ ), the applied load ( $L$ ), and the material hardness ( $H$ ), is given by Equation (1)<sup>[39,40]</sup>

$$W = k \times \frac{L}{H} \quad (1)$$

Equation (1) can be rearranged following the methodology proposed by Farhat et al. based on the formalism of the Hall-Petch expression, given by Equation (2)<sup>[41]</sup>

$$W = W_0 + k \times \left[ \frac{L}{H + aD^{-0.5}} \right] \quad (2)$$

where  $a$  is a constant, and  $D$  is the grain diameter. Equation (2) can be rearranged to encompass either  $\lambda_2$  or CGD by inserting the experimental hardness equations of Figure 5a–d, as shown in Figure 7a,b, respectively. As shown in Figure 7a, the wear rate decreases with the decrease in  $\lambda_2$ . Higher values of  $\lambda_2$  are related to coarser microstructures. A similar experimental equation obtained in a previous study by Reis et al. for as-cast 752 and 782 alloys is also shown in Figure 7a for comparison purposes.<sup>[23]</sup> A good agreement can be observed between the results, demonstrating the reproducibility of the analyses. Figure 7b shows the wear rate plotted as a function of CGD for the heat-treated alloys, and it is shown that  $W$  increases with the increase in CGD for both alloys. When the as-cast and the heat-treated results are compared, the 752 alloy shows a higher wear rate after heat treatment, despite the higher hardness and tensile strength achieved, evidencing that the effect of microstructure on the wear response is significant. By comparing the Vickers hardness (HV) variation from outside (Figure 5a,b) to inside (Figure 8) of the wear tracks, an increase from 80–102 to 151–166 HV was observed for the as-cast 752 alloy (a difference of about 60%), and approximately from 106–127 to 180–185 HV for the as-cast 782 alloy (a difference of about 50%), indicating that both alloys in the as-cast condition presented considerable strain hardening. After heat treatments, the variation in hardness at inside/outside of the wear tracks decreased gradually, as compared with the as-cast condition for the 752 alloy (from 120–128 to 171–180 HV—40%). For the 782 alloy, strain hardening decreased sharply in the

heat-treated condition (from 156–166 to 202–215 HV—30%). This behavior can clarify the changes in the wear rate of the 782 alloy, for which the wear resistance has been improved after heat treatment. In the as-cast condition, the experimental results have permitted obtaining a single equation for both alloys, whereas in the heat-treated condition the experimental tendencies were better demonstrated by one equation for each alloy.

SEM images of the wear-track surfaces of samples related to the position 50 mm from the cooled bottom for both alloys ingots are shown in Figure 8. The solid lines indicate that the wear track and details of some aspects of the worn surface are shown at the corners of the images. For the as-cast condition (Figure 8a), the presence of scratches, grooves, craters, and delamination in the 752 alloy was significantly more severe than that in the 782 alloy. After heat treatment (Figure 8b), the damages were more moderate for both alloys, for which the number of deep grooves and craters decreased, in special, for the 782 alloy.

In some regions, the compaction of the wear debris on the wear track causes the formation of shaped layers in all samples, as shown in the detailed areas. In both as-cast and heat-treated conditions, abrasive wear was the dominant wear mechanism. Pin damage was irrelevant in all conditions, and transfer of material to the pin occurred in all tests. Despite no metallurgical interaction between the pin and disc materials, adhesive wear damage was observed in some areas, probably due to interaction with the pin surface-transferred material.

## 4. Conclusions

The following major conclusions can be drawn from the present experimental study.

Hardness, tensile strength, and strain to fracture increased with the decrease in  $\lambda_2$  in the as-cast conditions of both examined alloys. After heat treatment, all these properties increased with the decrease in the CGD.

A solution time of about 3 h at 470 °C and an aging time of 4 h at 150 °C were shown to be the best conditions for the precipitation hardening heat treatment for both alloys.

Experimental equations are proposed, relating the resulting HB, UTS, and strain to fracture ( $\delta$ ) with microstructure

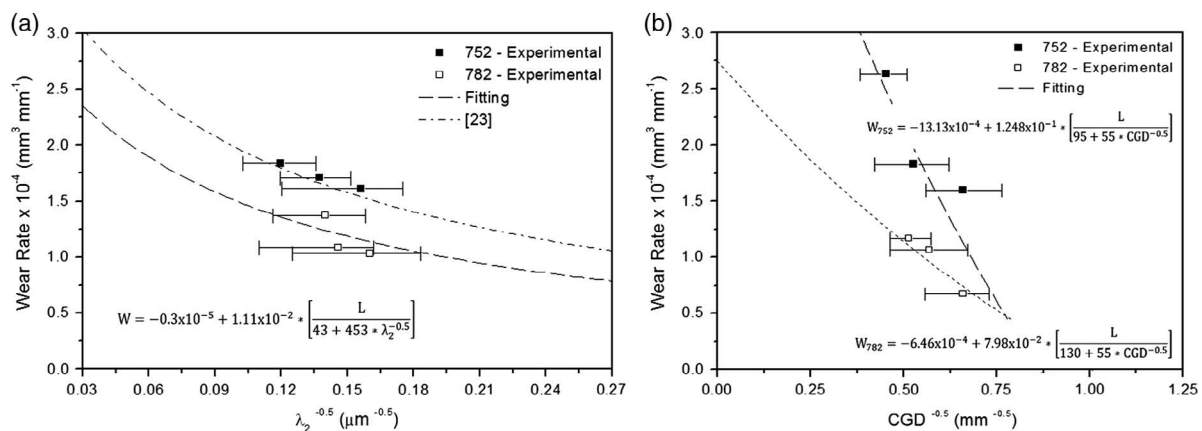


**Figure 7.** Wear rate variation with: a)  $\lambda_2$  for the as-cast condition and b) columnar grain size for the heat-treated condition.

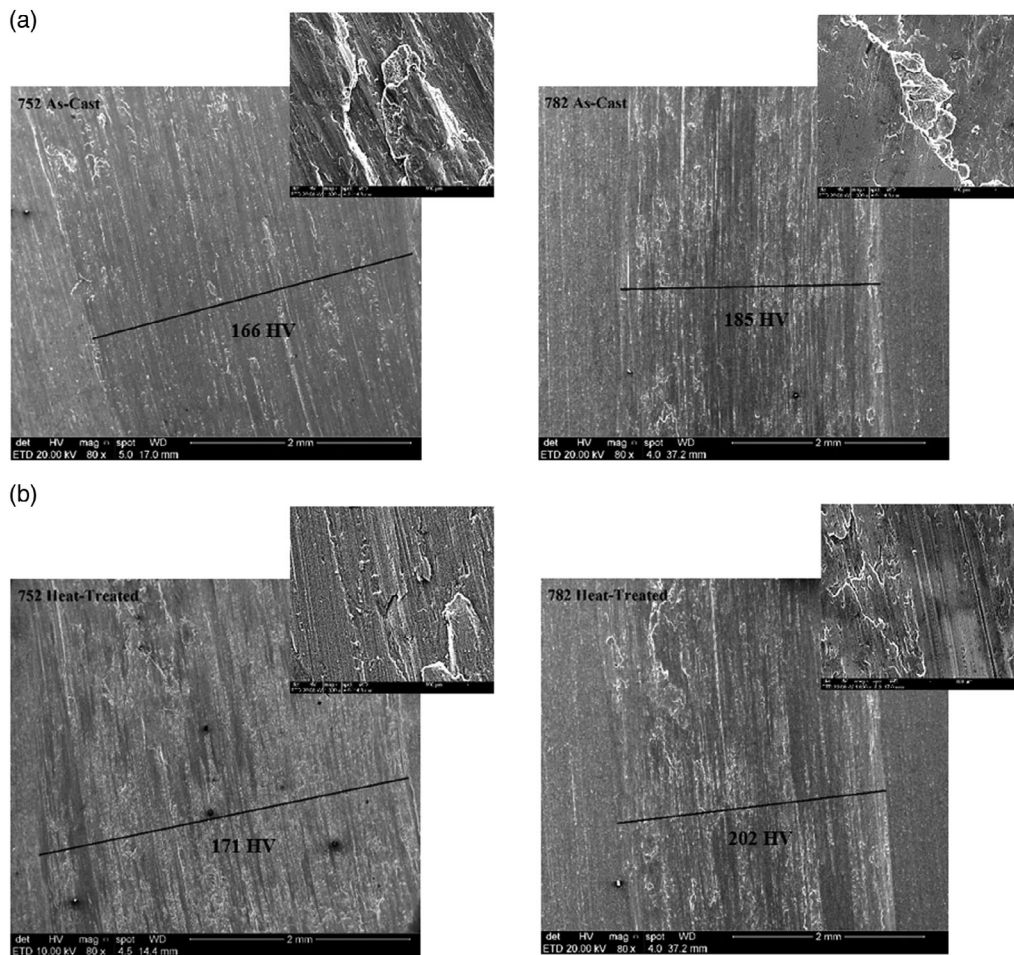


**Figure 8.** Wear-track surfaces of the 752 and 782 alloys in the: a) as-cast and b) heat-treated conditions. Position: 50 mm from the cooled bottom.

features:  $\lambda_2$  and CGD for the as-cast and heat-treated conditions, respectively.

The 752 alloy showed the poorest wear behavior in the heat-treated condition, whereas the 782 alloy presented the best wear response after heat treatment. In general, better wear resistance is associated with higher hardness and strength. However, depending on the microstructure features and contact aspects, wear resistance may have an opposite behavior inducing inappropriate material condition selection.

Correlations between wear rate ( $W$ ),  $\lambda_2$ , and CGD in the as-cast and heat-treated conditions were proposed, in which the wear rate decreases with decrease in  $\lambda_2$  and CGD and increase in the alloy Zn content.

The wear-track surfaces indicated that abrasive wear was the predominant wear mechanism.

## Acknowledgements

The authors acknowledge the support provided by National Council for Scientific and Technological Development (CNPq, grants: 403303/2016–8 and 301600/2015–5), Fundação de Amparo à Pesquisa do Rio Grande do Sul (FAPERGS), Coordenação de Aperfeiçoamento de

Pessoal de Nível Superior (CAPES), and Pontifícia Universidade Católica do Rio Grande do Sul (PUCRS).

## Conflict of Interest

The authors declare no conflict of interest.

## Keywords

Al–Mg–Zn alloys, mechanical properties, precipitation hardening, sliding wears, solidification

Received: September 23, 2019  
Revised: November 28, 2019  
Published online: January 27, 2020

- [1] T. Engdahl, V. Hansen, P. J. Warren, K. Stiller, *Mater. Sci. Eng. A* **2002**, 327, 59.
- [2] N. Belov, D. G. Eskin, A. Aksenov, *Multicomponent Phase Diagrams: Applications For Commercial Aluminum Alloys*, Elsevier, Amsterdam **2005**.

- [3] D. Dumont, A. Deschamps, Y. Brechet, *Mater. Sci. Eng. A* **2003**, 356, 326.
- [4] J. Gubicza, I. Schiller, N. Q. Chinh, J. Illy, Z. Horita, T. G. Langdon, *Mater. Sci. Eng. A* **2007**, 460–461, 77.
- [5] J. Zander, R. Sandstrom, *Mater. Des.* **2008**, 29, 1540.
- [6] E. Acer, E. Çadirli, H. Erol, T. Kirindi, M. Gündüz, *Mater. jrrSci. Eng. A* **2016**, 26, 144.
- [7] A. D. Isadare, B. Aremo, M. O. Adeoye, O. J. Olawale, M. D. Shittu, *Mater. Res.* **2013**, 16–1, 190.
- [8] A. K. Prasada Rao, K. Das, B. S. Murty, M. Chakraborty, *Wear* **2004**, 257, 148.
- [9] K. Lepper, M. James, J. Chashechkina, D. A. Rigney, *Wear* **1997**, 203–204, 46.
- [10] J. M. V. Quaresma, C. A. Santos, A. Garcia, *Metall. Mater. Trans. A* **2000**, 31, 3167.
- [11] J. E. Spinelli, D. M. Rosa, I. L. Ferreira, A. Garcia, *Mater. Sci. Eng. A* **2004**, 383, 271.
- [12] B. P. Reis, R. P. França, J. A. Spim, A. Garcia, E. M. Costa, C. A. Santos, *J. Alloys Compd.* **2013**, 549, 324.
- [13] P. R. Goulart, J. E. Spinelli, W. R. Osório, A. Garcia, *Mater. Sci. Eng. A* **2006**, 421, 245.
- [14] T. A. Costa, M. Dias, L. G. Gomes, O. L. Rocha, A. Garcia, *J. Alloys Compd.* **2016a**, 683, 485.
- [15] A. V. Rodrigues, T. S. Lima, T. A. Vida, C. Brito, A. Garcia, N. Cheung, *Met. Mater. Int.* **2018**, 24, 1058.
- [16] W. R. Osório, D. J. Moutinho, L. C. Peixoto, I. L. Ferreira, A. Garcia, *Electrochim. Acta* **2011**, 56, 8412.
- [17] K. S. Cruz, E. S. Meza, F. A. P. Fernandes, J. M. V. Quaresma, L. C. Casteletti, A. Garcia, *Metall. Mater. Trans. A* **2010**, 41, 972.
- [18] E. S. Freitas, J. E. Spinelli, L. C. Casteletti, A. Garcia, *Tribol. Int.* **2013**, 66, 182.
- [19] E. S. Freitas, A. P. Silva, J. E. Spinelli, L. C. Casteletti, A. Garcia, *Tribol. Lett.* **2014**, 55–1, 111.
- [20] T. A. Costa, M. Dias, E. S. Freitas, L. C. Casteletti, A. Garcia, *J. Alloys Compd.* **2016**, 689, 767.
- [21] F. Bertelli, E. S. Freitas, N. Cheung, M. A. Arenas, A. Conde, J. Damborenea, A. Garcia, *J. Alloys Compd.* **2017**, 695, 3621.
- [22] R. N. Rao, S. Das, D. P. Mondal, G. Dixit, *Tribol. Int.* **2010**, 43, 330.
- [23] B. P. Reis, M. M. Lopes, A. Garcia, C. A. Santos, *J. Alloys Compd.* **2018**, 764, 267.
- [24] ASTM E3-11 (2017), *Standard Guide For Preparation Of Metallographic Specimens*, ASTM International, West Conshohocken, PA **2011**.
- [25] ASTM E407-07 (2015), *Standard Practice For Microetching Metals And Alloys*, ASTM International, West Conshohocken, PA **2015**.
- [26] ASTM E112-13, *Standard Test Methods For Determining Average Grain Size*, ASTM International, West Conshohocken, PA **2013**.
- [27] ASTM E10-18, *Standard Test Methods For Brinell Hardness Of Metallic Materials*, ASTM International, West Conshohocken, PA **2018**.
- [28] ASTM G99-17, *Standard Test Method For Wear Testing With A Pin-On-Disk Apparatus*, ASTM International, West Conshohocken, PA **2017**.
- [29] ASTM E8/E8M-16a, *Standard Test Methods For Tension Test Of Metallic Materials*, ASTM International, West Conshohocken, PA **2016**.
- [30] V. Raghavan, *J. Phase Equilib. Diff.* **2007**, 28, 203.
- [31] O. Alvarez, C. Gonzalez, G. Aramburo, R. Herrera, J. A. Juarez-Islas, *Mater. Sci. Eng. A* **2005**, 402, 320.
- [32] J. Soto, G. Aramburo, C. Gonzalez, J. Genesca, R. Herrera, J. A. Juarez-Islas, *Mater. Sci. Eng. A* **2005**, 408, 303.
- [33] A. L. Ramirez-Ledesma, R. A. Rodríguez-Díaz, J. Chavez-Carvayar, O. Alvarez-Fregoso, J. A. Juarez-Islas, *Trans. Nonferrous Met. Soc. China* **2015**, 25, 1391.
- [34] D. Bouchard, J. S. Kirkaldy, *Metall. Mater. Trans. B* **1997**, 28, 633.
- [35] M. Chemingui, M. Khitouni, K. Jozwiak, G. Mesmacque, A. Kolsi, *Mater. Des.* **2010**, 31, 3134.
- [36] K. G. Prashanth, B. Debalina, Z. Wang, P. F. Gostin, A. Gebert, M. Calin, U. Kuhn, M. Kamaraj, S. Scudino, J. Eckert, *J. Mater. Res.* **2014**, 29, 2044.
- [37] K. G. Prashanth, S. Scudino, A. K. Chaubey, L. Lober, H. Attar, F. P. Schimansky, F. Pyczak, J. Eckert, *J. Mater. Res.* **2016**, 31, 55.
- [38] D. P. Mondal, S. Das, R. N. Rao, M. Singh, *Mater. Sci. Eng. A* **2005**, 402, 307.
- [39] J. F. Archard, *J. Appl. Phys.* **1953**, 24, 981.
- [40] J. F. Archard, W. Hirst, *Proc. R. Soc. A* **1956**, 236, 397.
- [41] Z. N. Farhat, Y. Ding, D. O. Northwood, A. T. Alpas, *Mater. Sci. Eng. A* **1996**, 206, 302.